AGU PUBLICATIONS

Geophysical Research Letters

RESEARCH LETTER
10.1002/2017GL075725

Key Points:
- A heterogeneous stress field is detected at the 2016 Kumamoto earthquake hypocentral area
- The expected slip direction from the estimated stress field correlates with the coseismic slip
- Highly pressured fluids around the fault enlarged the coseismic slip of the main shock

Supporting Information:
- Supporting Information S1
- Figure S1
- Figure S2
- Figure S3

Correspondence to:
S. Matsumoto,
matumoto@sevo.kyushu-u.ac.jp

Citation:
Matsumoto, S., Yamashita, Y., Nakamoto, M., Miyazaki, M., Sakai, S., Iio, Y., … Asano, Y. (2018). Prestate of stress and fault behavior during the 2016 Kumamoto earthquake (*M*7.3). *Geophysical Research Letters*, *45*, 637–645. https://doi.org/10.1002/2017GL075725

Received 22 SEP 2017
Accepted 21 DEC 2017
Accepted article online 29 DEC 2017
Published online 18 JAN 2018

Prestate of Stress and Fault Behavior During the 2016 Kumamoto Earthquake (*M*7.3)

Satoshi Matsumoto[1], Yusuke Yamashita[2], Manami Nakamoto[3], Masahiro Miyazaki[2], Shinichi Sakai[4], Yoshihisa Iio[2], Hiroshi Shimizu[1], Kazuhiko Goto[5], Tomomi Okada[6], Mako Ohzono[7], Toshiko Terakawa[8], Masahiro Kosuga[9], Masayuki Yoshimi[10], and Youichi Asano[11]

[1]Institute of Seismology and Volcanology, Kyushu University, Shimabara, Japan, [2]Disaster Prevention Research Institute, Kyoto University, Uji, Japan, [3]National Institute of Polar Research, Tokyo, Japan, [4]Earthquake Research Institute, University of Tokyo, Tokyo, Japan, [5]Graduate School of Science and Engineering, Kagoshima University, Kagoshima, Japan, [6]Graduate School of Science, Tohoku University, Sendai, Japan, [7]Graduate School of Science, Hokkaido University, Sapporo, Japan, [8]Graduate School of Environmental Studies, Nagoya University, Nagoya, Japan, [9]Graduate School of Science and Technology, Hirosaki University, Hirosaki, Japan, [10]Geological Survey of Japan, AIST, Tsukuba, Japan, [11]National Research Institute for Earth Science and Disaster Resilience, Tsukuba, Japan

Abstract Fault behavior during an earthquake is controlled by the state of stress on the fault. Complex coseismic fault slip on large earthquake faults has recently been observed by dense seismic networks, which complicates strong motion evaluations for potential faults. Here we show the three-dimensional prestress field related to the 2016 Kumamoto earthquake. The estimated stress field reveals a spatially variable state of stress that forced the fault to slip in a direction predicted by the "Wallace and Bott Hypothesis." The stress field also exposes the pre-condition of pore fluid pressure on the fault. Large coseismic slip occurred in the low-pressure part of the fault. However, areas with highly pressured fluid also showed large displacement, indicating that the seismic moment of the earthquake was magnified by fluid pressure. These prerupture data could contribute to improved seismic hazard evaluations.

Plain Language Summary The three-dimensional prestress field around the 2016 Kumamoto earthquake controlled fault behavior of the earthquake. The estimated heterogeneous state of stress on the fault forced the fault to slip in the direction predicted. The stress field also exposed the precondition of pore fluid pressure on the fault. Large coseismic slip occurred not only at the low-pressure part of the fault but also highly pressured part. It indicates that the seismic moment of the earthquake was magnified by fluid pressure. These prerupture data could contribute to upgrading seismic hazard evaluation.

1. Introduction

Earthquakes are governed by the state of stress and strength on a fault. Coulomb's failure criteria are often used when considering the occurrence of seismic activity (Jaeger et al., 2007), which demonstrate the relationship between shear strength, normal stresses, pore fluid pressure, and the friction coefficient on a fault. Once the state of stress at a point on the fault satisfies the criteria, the fault starts to slip, and rupture propagates to other parts of the fault. The slip characteristics of a fault depend on the conditions around the fault (Scholz, 2002). Knowing the controlling parameters of fault behavior is important for understanding earthquake mechanisms, and for further potential evaluation of destructive earthquakes. The recent development of seismic networks has enabled us to capture heterogeneous slip features on the faults of large earthquakes, and numerous studies have reported slip vectors for large earthquakes that changed direction and magnitude (Asano & Iwata, 2016; Hartzell & Heaton, 1983; Olson & Apsel, 1982). However, stress and pore fluid pressure conditions in the preearthquake stage are not always known due to a lack of seismic activity in the hypocentral area, which is used to estimate the stress field. The relationship between coseismic fault behavior and prestates, which depends on the stress and strength conditions characterized by fluid pressure, is important for understanding earthquake processes. In this study, we investigate this relationship for the 2016 Kumamoto earthquake; a recent and destructive event characterized by high preceding background seismic activity recorded by a dense seismic network.

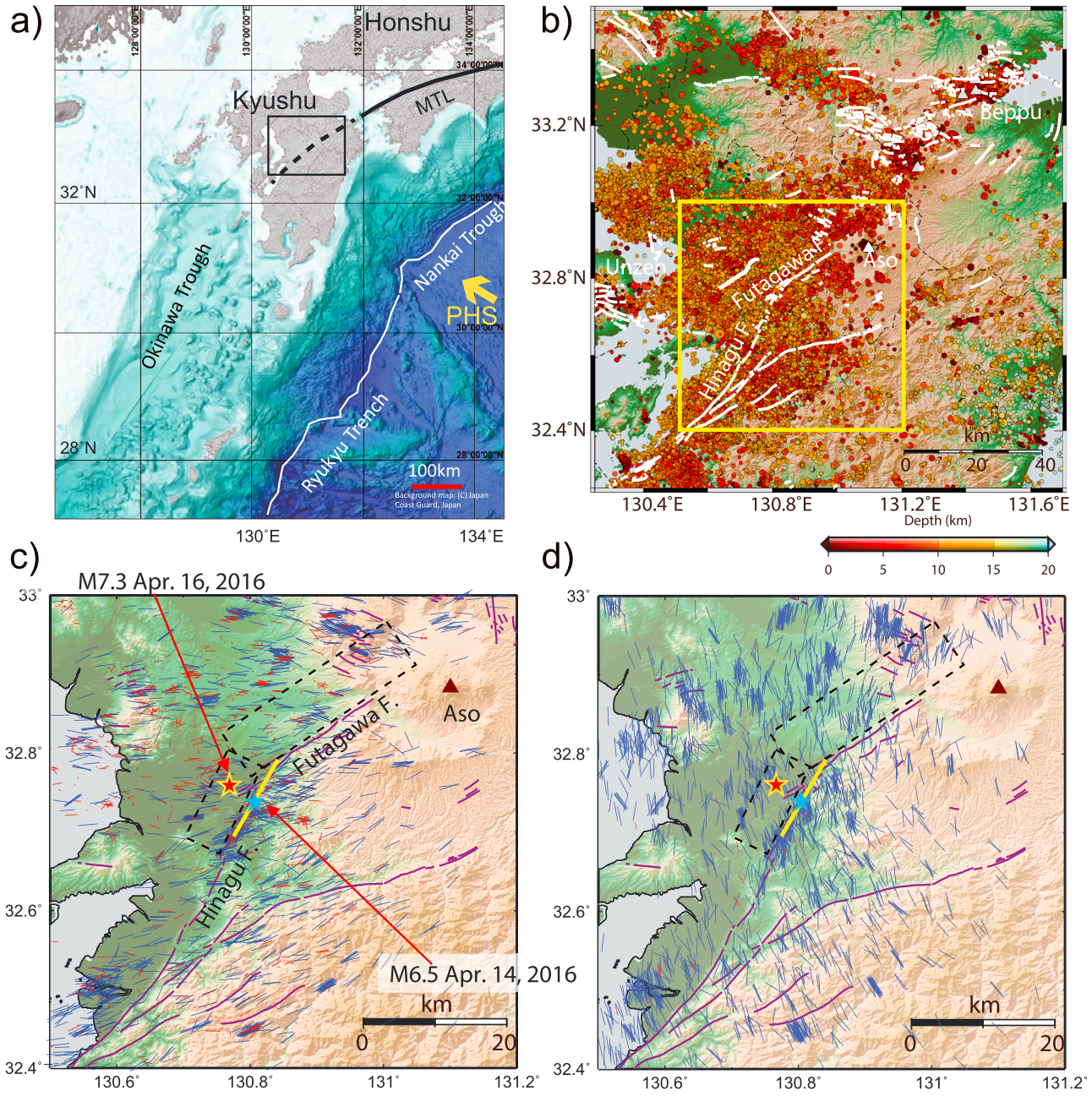

Figure 1. (a) Location map of Kyushu Island, southwestern Japan. The rectangle indicates the area shown in Figure 1b. (b) Hypocenter distribution around Hinagu and Futagawa fault systems for the 30 year period before the 2016 Kumamoto earthquake sequence. The yellow rectangle indicates the target area in this study. (c and d) *P* and *T* axes projected horizontal planes, respectively. Red segments in Figures 1c and 1d are axes with a dip angle greater than 45°. Dashed rectangles and yellow segment show the fault plane of the main shock and the largest foreshock, respectively (Asano & Iwata, 2016).

The 2016 Kumamoto earthquake (M_j7.3) occurred at 01:26 (all times in JST) on 16 April 2016 in Kumamoto prefecture, central Kyushu Island, Japan; the most seismically active area of Kyushu Island (Kato et al., 2016; Uchide et al., 2016). Figure 1 shows the location map of the hypocentral area. The sequence started with a large M_j6.5 foreshock (21:25, 14 April 2016) and was located around two active faults (the Futagawa and Hinagu faults). Many surface rupture traces appeared in the hypocentral area (Shirahama et al., 2016). Right-lateral slip of over 2 m was observed at the surface around the Futagawa fault. Coseismic fault behavior of the main shock and the largest foreshock were estimated by Asano and Iwata (2016) using strong motion records around the residential hypocentral area. They found a large slip area on a shallow part of the fault,

which could have been the cause of heavy damage in this area. In addition, their results showed complex fault behavior, with the main shock rupture growing not only through strike slip motion but also as normal faulting. Small earthquakes occurred along the active fault zone and over a wider area (Figure 1b). Stress fields for Kyushu Island were estimated by several studies (e.g., Terakawa & Matsu'ura, 2010; Matsumoto et al., 2015). The two-dimensional stress field of Kyushu Island (Matsumoto et al., 2015) showed characteristics consistent with (1) extension of the principal deviatoric stress in a N-S or NNW-SSE direction and (2) maximum compression close to the intermediate compression of central Kyushu Island. This suggests a uniaxial extensional stress regime. These stress conditions could be attributed to the complex rupture pattern of the main shock; however, the depth dependency and its role in coseismic faulting remains unclear.

Dense seismic observations were made in the hypocentral area before the earthquake by Kyushu and Kyoto Universities (Figure S1), and by additional stations deployed after the M_J6.5 earthquake in the hypocentral area by the Group for Urgent Seismic Observation of the 2016 Kumamoto earthquake (Shimizu et al., 2016). High-quality focal mechanism data from the dense seismic network have enabled us to estimate the stress field with high resolution. As described above, the Kumamoto area is one of the most seismically active on Kyushu Island. In this study, we investigated the three-dimensional stress field around the 2016 Kumamoto earthquake, and its relationship to coseismic rupture, using focal mechanism and seismic moment tensor data before the earthquake.

2. Data

We analyzed a data set of focal mechanisms from Kyushu Island from 1996 to 13 April 2016 (i.e., before the M_J6.5 earthquake). Data for shallow earthquakes (0–30 km) with magnitudes from 1.5 to 4 were selected because the detectability of the seismic network over this period was uniform, and large events are not applicable for the method used in this study. We determined focal mechanisms from *P* wave polarity data observed at eight or more stations using the HASH algorithm of Hardebeck and Shearer (2002). In total, 2,403 focal mechanisms characterized by a low misfit in the algorithm were obtained using the same criteria as that in Matsumoto et al. (2015). Figure 1 shows the *P* and *T* axis distributions used in this study. The method requires seismic moment tensor data to estimate the stress tensor. We created the data set using the empirical relationship between earthquake magnitude and the seismic moment tensor (Text S1 in the supporting information).

3. Heterogeneous Stress Field

3.1. Method

In a region loaded with triaxial maximum (σ_1), intermediate (σ_2), and minimum (σ_3) principal deviatoric stresses, the deviatoric stress tensor can be estimated from the summation of seismic moment tensors of earthquakes that have occurred in the target region based on plasticity theory (Matsumoto, 2016; see Text S2). Using constitutive relationships, the seismic moment density tensor is proportional to the deviatoric stress tensor; therefore, the deviatoric stress tensor in a medium deformed by many earthquakes can be obtained by the following formula:

$$\sigma_{ij} \propto \sum_k^K M_{ij}^k \tag{1}$$

where σ_{ij} is the deviatoric stress tensor, M_{ij}^k is the seismic moment tensor released by the *k*th earthquake in the target volume, and *K* is the number of earthquakes.

This formula means that the sum of the moment tensors for an earthquake within a given volume has a linear relationship with the deviatoric stress tensor. Although the magnitude of the stress tensor cannot be estimated, the total moment tensors in a volume provides the stress ratio ϕ $\left(\phi = \frac{\sigma_2 - \sigma_3}{\sigma_1 - \sigma_3}\right)$ and the principal stress directions, which is equivalent to the parameters of stress tensor inversion from focal mechanism data (e.g., Michael, 1984).

In this study, we estimated stress tensors in spatial blocks with a size of 0.075° in latitude and longitude, and 5 km in depth. The horizontal interval of the block was set to half the size of the block size (i.e., shifting 0.0375° in both horizontal directions). We set depth ranges of $0 < z \leqq 5$, $5 < z \leqq 10$, and $10 < z \leqq 15$ km, where *z* is depth. The spatial block analyzed in this study contained more than 10 events. The stress tensor was

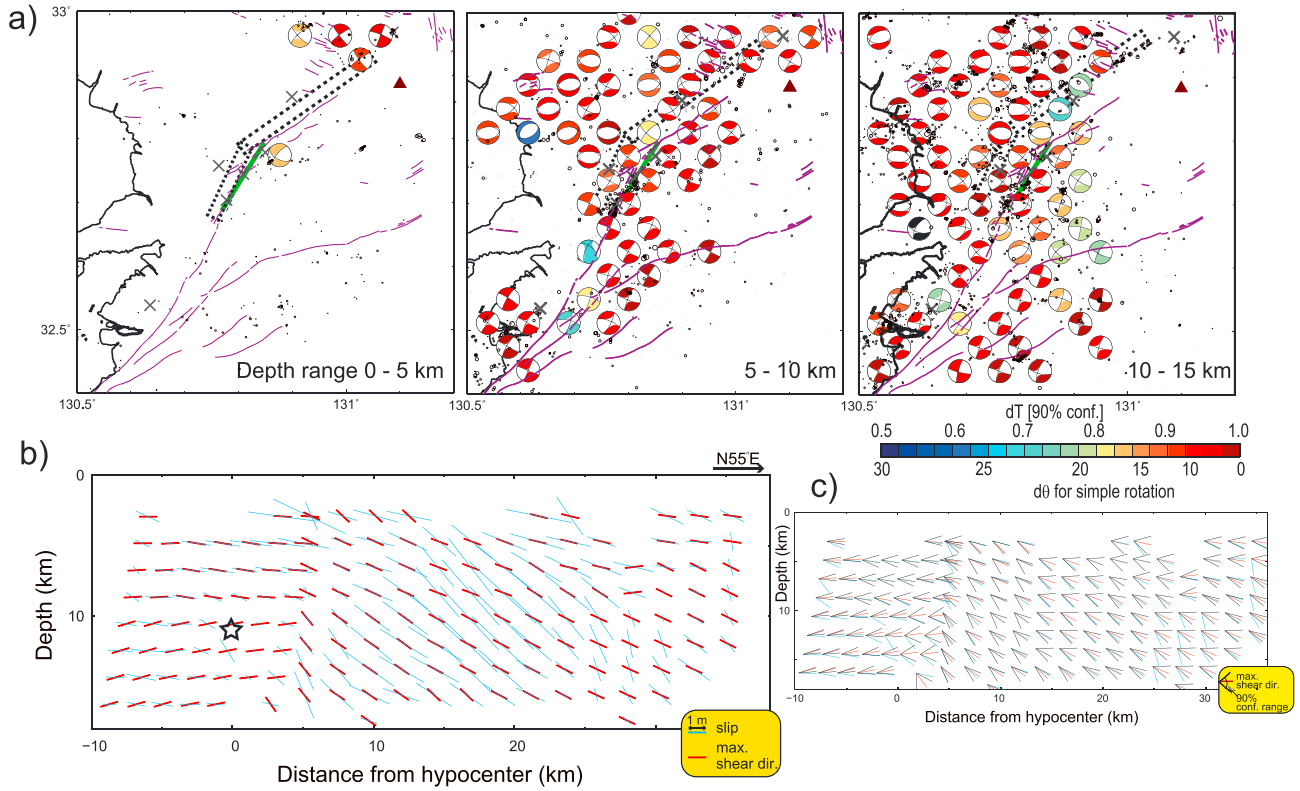

Figure 2. (a) Stress tensor distributions for three depth ranges. The tensor is plotted on the lower hemisphere of the focal sphere as the moment tensor. Color indicates the 90% confidence range of the tensor estimation scaled by tensor difference defined in the text. Tensor difference in degrees for rotation around the σ_2 axis is also indicated for reference. The dashed rectangle and green segment indicate the main shock and the largest foreshock fault in the depth range, respectively. (b) Rake angle distribution for the main shock plotted on the N55°E vertical plane. Expected slip direction of the main shock from the stress tensor (red) and the coseismic slip (blue) of Asano and Iwata (2016) are also displayed. (c) Expected slip direction with a 90% confidence range.

independently estimated from earthquakes occurring in each block. A 90% confidence range for each parameter was evaluated using a bootstrap resampling test. The range is evaluated from the discrepancy between the solution from the resampling data set (m'), within 90% of the total number in the test, and the optimum tensor (m), which is expressed using the tensor product (dT; Terakawa, 2017). The product is defined as

$$\mathrm{d}T(m,m') = \sum_{i=1}^{3}\sum_{j=1}^{3} m_{ij}m'_{ij} \Big/ \sqrt{\sum_{i=1}^{3}\sum_{j=1}^{3} m_{ij}{}^2}\sqrt{\sum_{i=1}^{3}\sum_{j=1}^{3} m'_{ij}{}^2} \tag{2}$$

3.2. Stress Field

The estimated stress tensors are plotted in Figure 2 for depth ranges of 0–5, 5–10, and 10–15 km. The 90% confidence range for each parameter was evaluated using the bootstrap resampling test and the beach ball color scale (Figure 2). The stress tensors at the depth shallower than 5 km are not well constrained. General features of the stress field are similar to the results of Matsumoto et al. (2015). The σ_3 axes in the target area are horizontal and their azimuths are NNW-SSE or N-S. The σ_3 axes are oriented N-S around the Hinagu and Futagawa faults. In contrast with the stable σ_3 axis, reliable σ_1 and σ_2 directions reveal spatial variation. Blocks with horizontal σ_1 (i.e., strike slip stress regimes) are found around shallow parts of the fault. However, vertical σ_1 vectors are found at grids in the northwestern part of the target region. This feature is remarkable in the deep part of the fault, indicating a region under a normal stress regime. The intermediate stress vectors show features complementary to those for σ_1. Spatial changes in the stress regime, which transitions from strike slip to normal faulting when moving from southeast to northwest, suggests a decline in σ_1 toward the northwest. Figure 2a shows the coseismic fault of the main shock, as presented by Asano and Iwata (2016). The dashed rectangle for each depth range indicates the existing coseismic fault. The stress regimes in blocks around the main shock fault show important characteristics that indicate depth dependency. The principal

stress direction also shows spatial variation around the main shock fault. The heterogeneous stress field around the source fault of the main shock suggests that coseismic rupture might have been affected by the stress field.

3.3. Relationship to Coseismic Fault Behavior

We obtained the heterogeneous stress field not only in the lateral direction but also with depth prior to the main shock. We defined a maximum shear stress direction on the fault (hereafter the Max-SSDF) that is a projection of the traction vector on the fault plane. Max-SSDF can be calculated from the stress field and fault geometry, which provides the expected slip direction of an earthquake on a given fault. We adopted the fault geometry of Asano and Iwata (2016) (see also Text S3), who considered two fault planes with strike/dip angles of 205/72° and 235/65° to explain strong motion records for the main shock. The slip vectors have been estimated as 2 × 2 km subfaults on the two faults. Therefore, Max-SSDF at the center of each subfault is calculated from the fault geometry and the estimated stress tensor of the closest block less than 5 km away. Figure 2b shows the rake angle distribution of the Max-SSDF projected on the N55E vertical plane.

According to Asano and Iwata (2016), the maximum slip of the main shock reached over 6 m, and the total released seismic moment was 4.50×10^{19} Nm (M_w7.0). The major coseismic slip occurred in the middle of the fault, and its direction was not uniform. The fault involved both strike slip and normal slip along the Futagawa fault. Figure 2b also shows their coseismic slip.

In this study, we noted two depth ranges (5–10 and 10–15 km) because the spatial blocks cover the entire coseismic fault within these ranges. We found similarities between the coseismic slip and the Max-SSDF (Figure 2b). Strike slip on the coseismic fault was detected on the southwest part of the fault, where horizontal Max-SSDF was also estimated. In the middle part of the fault, Max-SSDF changed direction, resulting in a normal faulting component. Then, the real fault exhibited slip oblique to the horizontal plane. More than 85% of the subfaults showed that the residual angle of the coseismic fault from the optimum value of the Max-SSDF was smaller than 30°. This Max-SSDF change from the SW of the fault to the central part of the fault is reliable within a 90% confidence range. As described above, Max-SSDF estimation only used earthquakes that occurred prior to the Kumamoto earthquake sequence. This is important because it implies that we can predict slip direction on a fault before a large earthquake occurs, if accurate fault geometry is known. Wallace (1951) and Bott (1959) hypothesized that fault slip is controlled by the maximum shear stress direction, and this assumption is commonly adopted in stress tensor inversion (e.g., Michael, 1984, 1987). The results of this study confirm this assumption in the case of natural earthquake faulting during large earthquakes. In addition, the correlation between Max-SSDF and coseismic slip direction was observed for the largest foreshocks (Figure S2); therefore, we conclude that the fault behavior of the Kumamoto earthquake is attributable to a complex stress field. Although other studies have highlighted the relationship between stress and coseismic slip direction on active faults (e.g., Terakawa & Matsu'ura, 2010; Yukutake et al., 2015), this study is the first to show that for a large natural earthquake, the prestate of stress on the fault controls the slip direction of complicated coseismic fault slip.

4. Unfavorable Fault Orientation Under Stress Conditions and Fluid Pressure

The heterogeneous stress field and coseismic fault geometry enable us to discuss whether fault orientation has an optimum direction under Coulomb failure criteria. Slip generation on unfavorably oriented faults requires a decrease in fault strength, for example, by raising pore fluid pressure. Stress tensor estimation using moment tensor data can only solve for the shape of the deviatoric stress tensor (i.e., the direction of the principal stress axes and stress ratio). However, the tensor structure and fault plane geometry provide shear and normal stresses normalized by maximum shear stress. According to the Coulomb failure criteria, fault slip occurs if shear stress τ reaches the strength composed of cohesive strength τ_0, the friction coefficient μ, normal stress σ_n, and the pore fluid pressure p

$$\tau = \tau_0 + \mu(\sigma_n - p) \tag{3}$$

Using the expressions below, we define a normalized Mohr diagram (Figure 3a):

$$\tau' = \frac{\tau}{\tau_{max}}, \quad \tau_{max} = \frac{\sigma_1 - \sigma_3}{2} \sigma_n' = \left(\sigma_n - \frac{(\sigma_1 + \sigma_3)}{2}\right) / \tau_{max} \tag{4}$$

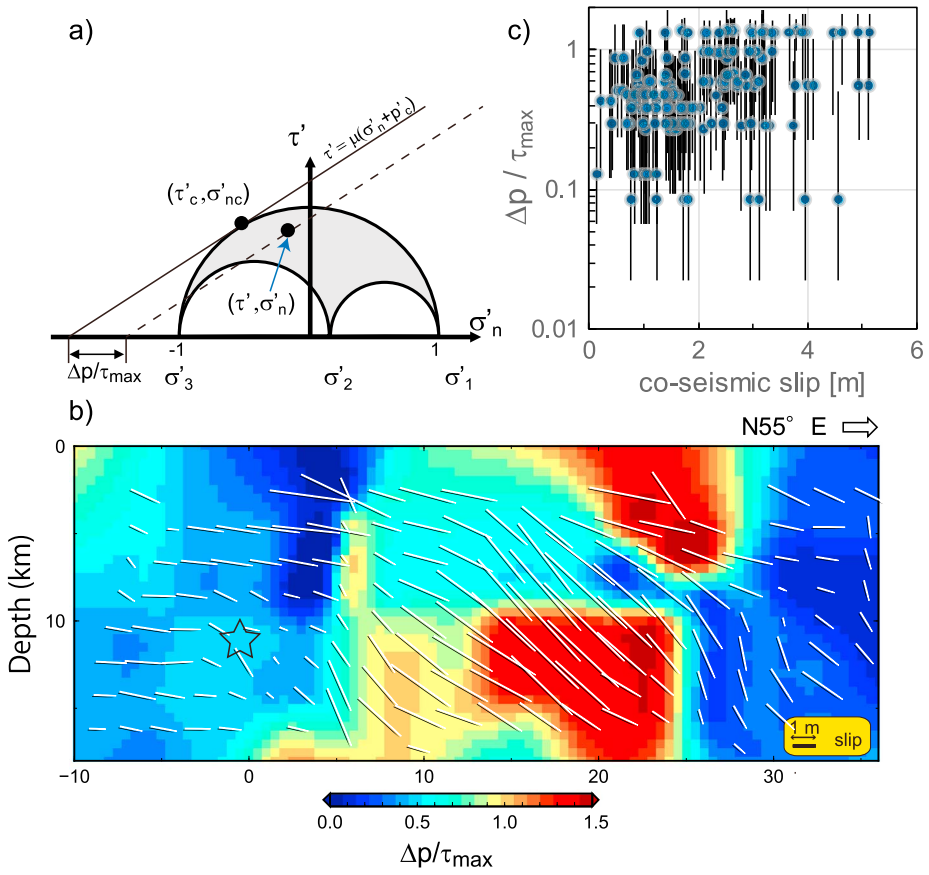

Figure 3. (a) Schematic of relative pore fluid pressure estimate in a unit Mohr diagram. The diagram is normalized by τ_{max}. The earthquake occurs on an optimum oriented fault plane under Coulomb failure criteria at shear and normal stress (τ'_c, σ'_{nc}). Relative pressure is measured from the pore fluid pressure required for failure on the optimum plane and normalized by τ_{max}. (b) Relative pore fluid pressure $\Delta p/\tau_{max}$ on the main shock fault as projected on the N55°E vertical plane. Segments are the coseismic slip of Asano and Iwata (2016). The star shows the hypocenter of the main shock. (c) $\Delta p/\tau_{max}$ versus the coseismic slip of the main shock. The error bar indicates the 90% confidence range for the estimate.

In the diagram, the maximum and minimum principal stresses become $\sigma'_1 = 1$, $\sigma'_3 = -1$, and maximum shear stress $\tau'_{max} = \tau_{max}/\tau_{max} = 1$. Values of σ'_n and τ' can be calculated from the stress tensor and assumed fault plane. The line satisfying the Coulomb failure criteria touches the diagram at (τ'_c, σ'_{nc}), where $\tau'_c = \frac{1}{\sqrt{1+\mu^2}}, \sigma'_{nc} = -\frac{\mu}{\sqrt{1+\mu^2}}$. A point crossing the line on the σ_n' axis corresponds to the normalized pore fluid pressure ($p'_c = p_c/\tau_{max}$), where p_c is the pore fluid pressure for failure of an optimally oriented fault. An optimum fault orientation is determined by the frictional coefficient and the stress tensor. According to Terakawa et al. (2012), and Terakawa and Matsu'ura, (2010), pore fluid pressure can be estimated from the stress field and fault plane geometry. They revealed excess fluid pressure and discussed its relationship with earthquake magnitude. Relative pore fluid pressure $\Delta p' = \Delta p/\tau_{max} = (p - p_c)/\tau_{max}$ can be defined by the formula

$$\Delta p' = \sigma' - \sigma'_{nc} - \frac{\tau' - \tau'_c}{\mu} = \sigma' - \frac{\tau'}{\mu} + \frac{\sqrt{1+\mu^2}}{\mu} \quad (5)$$

The strength can be described by $\Delta p'$. This $\Delta p'$ corresponds to the overpressure coefficient introduced by Terakawa et al. (2012).

The τ' and σ' plotted on a unit Mohr diagram reveal the strength on the part of the fault at which the earthquake occurs. Figure 3a shows the relationship between the criteria and $\Delta p'$ in the unit Mohr diagram. The $\Delta p'$ distribution for the main shock fault was calculated from the coseismic fault geometry and stress tensor distribution, as displayed in Figure 3b. To estimate the values, we adopted $\mu = 0.6$ in equation (4) as a typical

frictional coefficient (Byerlee, 1978). Note that because we only used data from before the Kumamoto earthquake sequence, the main shock occurred on a fault with a heterogeneous $\Delta p'$ distribution (Figure 3b). High $\Delta p'$ indicates unfavorable coseismic fault orientation under the estimated stress field. From Figure 3b, we can see that large coseismic slip occurred on a portion of the fault that not only has a favorable oriented (low $\Delta p'$) but also areas of unfavorable orientation (high $\Delta p'$ over the maximum shear stress). The relationship between $\Delta p'$ and coseismic slip is displayed in Figure 3c. Fault areas with small slip show various $\Delta p'$. In contrast, two major pressure conditions were observed at larger slip regime, low (close to zero) and high (more than the maximum shear stress). The fault area with $\Delta p'$ of higher than τ_{max} released approximately 25% of the total seismic moment of the main shock. The cause of the heterogeneous $\Delta p'$ distribution is attributable to two factors: (1) nonuniform fluid pressure distribution and/or (2) heterogeneous differential shear stress.

For case (1), from the point of view of spatial fluid pressure variation, the large slip area with low $\Delta p'$ appears to have high strength because a fault with high strength can be loaded with high stress and can generate large slip to release the accumulated stress. According to an observational study by Terakawa et al. (2012), seismic moment increases with decreasing pore fluid pressure (i.e., increasing fault strength). In Figure 3b, the rupture of the main shock was initiated at the hypocenter and expanded toward another fault area with a different strike angle. The large slip area on the fault extended from the upper western edge to the middle part. Most of the large slip occurred along areas of low fluid pressure. In addition, the largest foreshock fault occurred under low-pressure conditions, indicating a "normal" earthquake, as shown in Figure S2c. In contrast, we found an area with high $\Delta p'$ hosted large slip displacement. Usually, low-strength faults caused by high pore fluid pressure are not able to create large slip because of a lower capacity for elastic strain energy for stress loading. We consider that the high strength fault area sustained stress loading over the entire fault. In this case, the low strength fault area maintained those conditions without slip until the event, and experienced similar displacement to the high strength area. We also consider the following additional possibilities: (a) that high fluid pressure could contribute to fault weakening such as thermal pressurization (Scholz, 2002; Sibson, 1973) during coseismic slip and (b) that rupture propagated into the low stress, weak area (high $\Delta p'$) due to rupture dynamics, and the low stress hindered the progress of the rupture. Our observational results suggest that strength heterogeneity on the fault enabled a large amount of slip in low strength areas. High pore fluid pressure may also contribute to enlarging earthquake faulting and/or stopping rupture.

For case (2), we consider constant Δp in the target area (i.e., uniform strength on the fault). Apparent $\Delta p'$ distribution can be produced by τ_{max} heterogeneity. The stress ratio and stress regime variations in this study indicated spatial τ_{max} heterogeneity. Therefore, we consider whether the stress heterogeneity is sufficient to create the obtained $\Delta p'$ variation (see also Text S5). We evaluated the $\Delta p'$ change due to a stress model that maximum compressional stress decreased with increasing stress ratio from the pure strike slip regime. This regime was found around the Hinagu fault area. As shown in Figure S3, we observed separation of fluid pressure on two large slip areas. This indicates heterogeneous fault strength (i.e., the case 1; nonuniform fluid pressure) and large slip on the weak part of the fault.

5. Discussion

The estimated stress field in the target area exhibits three-dimensional heterogeneous features. Lateral variations in the stress regime, which change from a strike-slip stress regime to a normal fault stress regime in the northern section of the Futagawa fault, could be attributable to a decline in the horizontal compressional stress, as suggested by Matsumoto et al. (2015). They considered that the change was caused by a relaxation of stress in the E-W direction around the anomalous contraction zone of Aso volcano, as detected by Global Navigation Satellite System (GNSS) analysis. In this study, we detected stress variations with depth. One possible interpretation is that the over burden pressure increases with depth of the medium. Increments of the vertical stress results show that the vertical stress might have been close to the maximum horizontal stress. This can be seen as domination of the non-double-couple component in stress tensors in the 10–15 km depth range (Figure 2a).

Some areas show a significant discrepancy between MAX-SSDF and the coseismic slip at the segment boundaries, suggesting strongly heterogeneous stress conditions due to rupture termination. Specifically, subfaults with large misfits were identified around the northeastern part of the fault (Figure 2b). This likely reflects the

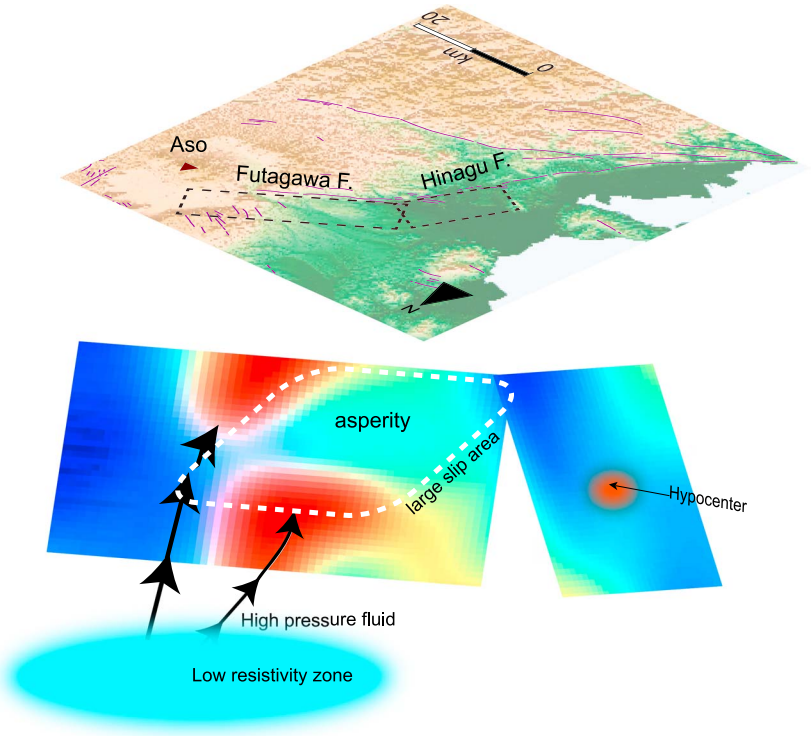

Figure 4. Conceptual illustration for weak and high-strength areas of the main shock fault. Red to blue color shows the degree of strength. Weaker areas (red color) might be fluid supplied from adjacent low-resistivity zones. Large slip occurs not only in high-strength areas (blue color, asperity) but also in low-strength areas.

fact that the northeastern part of the fault corresponds to the caldera Aso volcano, which exhibits a low-velocity zone and deformation source associated with volcanic activity (Abe et al., 2017). The coseismic rupture terminated at the caldera (Asano & Iwata, 2016). Seismic rupture around the edge of a fault generally creates a complex stress profile. In addition, the complex structures relating to Aso volcano might disturb the stress field. Another possibility is that dynamic stress forces changes in the coseismic slip direction, as seen in the 1995 Kobe earthquake (Guatteri & Spudich, 1998).

Fluid pressure is known to induce seismic activity (e.g., Terakawa et al., 2012). In this study, we show how a heterogeneous fluid pressure distribution could have contributed to expanding the large slip area during the Kumamoto earthquake. In order to supply high-pressure fluid to the hypocentral area, fluid flow from outside would have been required. Aizawa et al. (2017) estimated the resistivity structure in and around the target area. They found a relatively low-resistivity area distributed north of the Futagawa fault, extending to at least 20 km depth and apparently bounded by the fault. This low-resistivity area reflects the existence of fluid flow, suggesting a pathway along which fluid is supplied to the hanging wall of the fault. Values of $^{3}He/^{4}He$ are higher in the fault area (National Institute of Advanced Industrial Science and Technology, 2017, https://unit.aist.go.jp/ievg/crufluid-rg1/kumamoto/kumamoto.html), which also implies a path for transporting material from the lower crust. Figure 4 schematically illustrates the main shock fault of the 2016 Kumamoto earthquake. The fault rupture started at the hypocenter in the southern segment and then propagated to the north where it created large slip along high-strength areas (i.e., commonly called "asperities"). The dynamic rupture producing the large slip in the asperity extended to the areas with high fluid pressure surrounding the asperity.

6. Conclusions

In this study, we estimated a regional three-dimensional stress field from moment tensor data of earthquakes that occurred before the 2016 Kumamoto earthquake sequence. We used our results to consider coseismic fault behavior during the earthquake and found the following:

1. Lateral heterogeneous and depth-dependent stress fields were dominant.
2. Coseismic fault behavior (slip direction) followed the prestate of stress, exhibiting heterogeneous features around the fault zone.
3. Approximately 25% of the seismic moment release was from the weakest part ($\Delta p > \tau_{max}$) of the fault.

The results of this study suggest that slip direction of co-seismic faulting can be evaluated from stress and fluid pressure conditions prior to large earthquakes. These findings will contribute to advancing strong motion evaluations for large earthquake faults.

Acknowledgments
We are grateful to Newman and two anonymous reviewers for their helpful comments and suggestions. We used focal mechanism data from Matsumoto et al. (2015) and Shimizu et al. (2016). Moment tensor data were obtained from the F-net catalog (URL: http://www.fnet.bosai.go.jp/event/search.php?LANG=en). We are grateful to the Group for Urgent Joint Seismic Observations of the 2016 Kumamoto Earthquake, and to Kyushu, Kyoto, and Kagoshima Universities, NIED, and JMA for providing high-quality data for use in this study. This study was supported by the Ministry of Education, Culture, Sports, Science and Technology (MEXT) of Japan, under its Earthquake and Volcano Hazards Observation and Research Program and MEXT KAKENHI (grants 26109004 and 16H05298). There are no conflicts of interest to declare.

References

Abe, Y., Ohkura, T., Shibutani, T., Hirahara, K., Yoshikawa, S., & Inoue, H. (2017). Low-velocity zones in the crust beneath Aso caldera, Kyushu, Japan, derived from receiver function analyses. *Journal of Geophysical Research: Solid Earth*, *122*, 2013–2033. https://doi.org/10.1002/2016JB013686

Aizawa, K., Asaue, H., Koike, K., Takakura, S., Utsugi, M., Inoue, H., … Shimizu, H. (2017). Seismicity controlled by resistivity structure: The 2016 Kumamoto earthquakes, Kyushu Island, Japan. *Earth, Planets and Space*, *69*(1), 4. https://doi.org/10.1186/s40623-016-0590-2

Asano, K., & Iwata, T. (2016). Source rupture processes of the foreshock and mainshock in the 2016 Kumamoto earthquake sequence estimated from the kinematic waveform inversion of strong motion data. *Earth, Planets and Space*, *68*(1), 147. https://doi.org/10.1186/s40623-016-0519-9

Bott, M. H. P. (1959). The mechanics of oblique slip faulting. *Geological Magazine*, *96*(2), 109–117. https://doi.org/10.1017/S0016756800059987

Byerlee, J. (1978). Friction of rocks. *Pure and Applied Geophysics*, *116*(4-5), 615–626. https://doi.org/10.1007/BF00876528

Guatteri, M., & Spudich, P. (1998). Coseismic temporal changes of slip direction: The effect of absolute stress on dynamic rupture. *Bulletin of the Seismological Society of America*, *88*, 777–789.

Hardebeck, J. L., & Shearer, P. M. (2002). A new method for determining first-motion focal mechanisms. *Bulletin of the Seismological Society of America*, *92*(6), 2264–2276. https://doi.org/10.1785/0120010200

Hartzell, S. H., & Heaton, T. (1983). Inversion of strong ground motion and teleseismic waveform data for the fault rupture history of the 1979 Imperial Valley, California, earthquake. *Bulletin of the Seismological Society of America*, *73*, 1553–1583.

Jaeger, J. C., Cook, N. G. W., & Zimmerman, R. W. (2007). *Fundamentals of rock mechanics 4th edition*. Oxford, UK: Blackwell Publishing Ltd.

Kato, A., Fukuda, J., Nakagawa, S., & Obara, K. (2016). Foreshock migration preceding the 2016 M_w 7.0 Kumamoto earthquake, Japan. *Geophysical Research Letters*, *43*(17), 8945–8953. https://doi.org/10.1002/2016GL070079

Matsumoto, S. (2016). Method for estimating the stress field from seismic moment tensor data based on the flow rule in plasticity theory. *Geophysical Research Letters*, *43*(17), 8928–8935. https://doi.org/10.1002/2016GL070129

Matsumoto, S., Nakao, S., Miyazaki, T. O. M., Shimizu, H., Abe, Y., Inoue, H., … Yamashita, Y. (2015). Spatial heterogeneities in tectonic stress in Kyushu, Japan and their relation to a major shear zone. *Earth, Planets and Space*, *67*(1), 172. https://doi.org/10.1186/s40623-015-0342-8

Michael, A. J. (1984). Determination of stress from slip data: Faults and folds. *Journal of Geophysical Research*, *89*(B13), 11,517–11,526. https://doi.org/10.1029/JB089iB13p11517

Michael, A. J. (1987). Use of focal mechanisms to determine stress: A control study. *Journal of Geophysical Research*, *92*(B1), 357–368. https://doi.org/10.1029/JB092iB01p00357

Olson, A. H., & Apsel, R. J. (1982). Finite faults and inverse theory with applications to the 1979 Imperial Valley earthquake. *Bulletin of the Seismological Society of America*, *72*, 1969–2001.

Scholz, C. H. (2002). *The mechanics of earthquakes and faulting*. Cambridge, UK: Cambridge University Press. https://doi.org/10.1017/CBO9780511818516

Shimizu, H., Iio, Y., Sakai, S., Okada, T., Takahashi, H., Watanabe, T., … Kurashimo, E. (2016). Urgent joint seismic observation of the 2016 Kumamoto earthquake—Seismic activities and their background, Abstract of Japan Geoscience Union 2016 Meeting.

Shirahama, Y., Yoshimi, M., Awata, Y., Maruyama, T., Azuma, T., Miyashita, Y., … Asahina, D. (2016). Characteristics of the surface ruptures associated with the 2016 Kumamoto earthquake sequence, central Kyushu, Japan. *Earth, Planets and Space*, *68*, 191. https://doi.org/10.1186/s40623-016-0559-1

Sibson, R. H. (1973). Interactions between temperature and fluid pressure during earthquake faulting—A mechanism for partial or total stress relief. *Nature*, *243*, 66–68.

Terakawa, T. (2017). Overpressurized fluids drive microseismic swarm activity around Mt. Ontake volcano, Japan. *Earth, Planets and Space*, *69*(1), 87. https://doi.org/10.1186/s40623-017-0671-x

Terakawa, T., & Matsu'ura, M. (2010). The 3-D tectonic stress fields in and around Japan inverted from centroid moment tensor data of seismic events. *Tectonics*, *29*, TC6008. https://doi.org/10.1029/2009TC002626

Terakawa, T., Miller, S. A., & Deichmann, N. (2012). High fluid pressure and triggered earthquakes in the enhanced geothermal system in Basel, Switzerland. *Journal of Geophysical Research*, *117*, B07305. https://doi.org/10.1029/2011JB008980

Uchide, T., Horikawa, H., Nakai, M., Matsushita, R., Shigematsu, N., Ando, R., & Imanishi, K. (2016). The 2016 Kumamoto-Oita earthquake sequence: Aftershock seismicity gap and dynamic triggering in volcanic area. *Earth, Planets and Space*, *68*(1), 180. https://doi.org/10.1186/s40623-016-0556-4

Wallace, R. E. (1951). Geometry of shearing stress and relation of faulting. *Journal of Geology*, *59*(2), 118–130. https://doi.org/10.1086/625831

Yukutake, Y., Takeda, T., & Yoshida, A. (2015). The applicability of frictional reactivation theory to active faults in Japan based on slip tendency analysis. *Earth and Planetary Science Letters*, *411*, 188–198. https://doi.org/10.1016/j.epsl.2014.12.005